

Reviewer 1:

The revised manuscript has made significant improvements. A few remaining questions for clarification:

Line 86-90: Are cloud properties retrieved on its native MODIS/VIIRS resolution and then converted into CERES footprint or the radiances are converted into CERES footprint resolution first and then applied with cloud retrieval algorithm? If the latter, mention radiance then cloud property.

*The cloud properties are retrieved on the native MODIS/VIIRS resolution, then averaged into the CERES footprint.*

Line 164-167: The FM3 and FM5 response to LW seems to explain the NPP LW radiance smaller compared to Aqua LW radiance. But SW responses of FM3 and FM5 seem contradictory to the observed radiance differences.

*What we discussed on lines 164-167 is the normalized instrument gains for each CERES FM3 and FM5 since the beginning of the mission. The changes provided are relative to the beginning of the mission for each instrument, or the relative changes over the years. The relative change of each instrument is different from the absolute differences shown in Figure 1.*

Figure 6: Based on my understanding, VIIRS-like cloud would only affect the choice of ADM, not the generation of NB radiance for NPP footprint size and the conversion from NB to BB radiance. If this is the case, the right branch of the procedure for NPP with VIIRS-like retrieval is not accurate. Do step one and step two affected by cloud?

*The reviewer is correct, the VIIRS-like cloud would only affect the selection of ADMs, but not the MODIS NB radiances and the conversion from NB to BB radiances. Figure 6 is modified accordingly and text describing the figure is also modified. Thank you for pointing this out.*

Reviewer 2:

Overall comment:

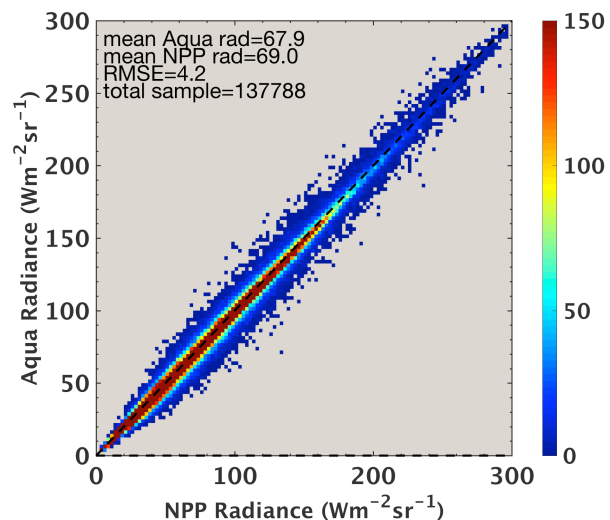
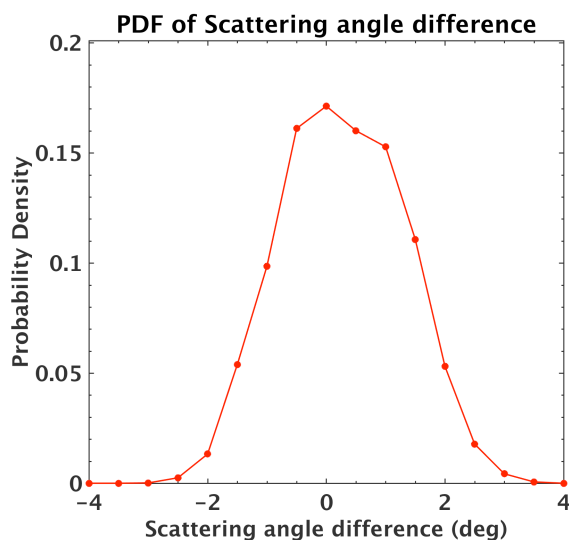
The manuscript has much improved from the first version I reviewed. However I still have a few concerns that I would like the authors to address.

Major comments:

Beginning of Section 2: you guys still haven't explained why you didn't use the scattering angle differences in your pixel matching algorithm. It's the scattering angle that really matters when comparing VIIRS and MODIS. When you do individual angle thresholds the differences can add up constructively and you end up with a large scattering angle difference, larger than you'd want to have in any case.

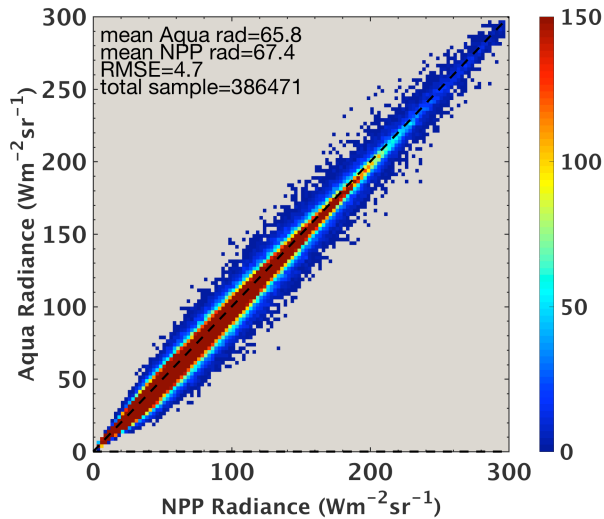
Please evaluate the scattering angle differences between MODIS and VIIRS in your selected footprints. Differences in individual zenith/azimuth angles can add up constructively and create significant scattering angle differences.

*As we explained in our first round response,  $\cos(\text{scattering angle}) = \cos((\text{SZA})\cos(\text{VZA}) + \sin(\text{SZA})\sin(\text{VZA})\cos(\text{RAZ}))$ . The SW radiance matching criteria used for Fig. 1 and Table 1 are that latitude and longitude differences are less than 0.05 degree, and the SZA difference is less than 2 degrees, VZA difference is less than 2 degrees, and the relative azimuth angle difference is less than 5 degrees. To answer the reviewer's concern, we calculated the scattering angle differences between matched Aqua and NPP footprints. The PDF of the scattering angle differences is shown below on the left and the scattering angle differences are less than 2° for about 95.6% of the matched footprints and are less than 3° for about 99.9% of the matched footprints. We added on page 7 that the criteria we used also provide tight constraint on scattering angle. When we added the scattering angle difference < 2° to the matching criteria, the SW result (shown below on the right) is very similar to that in Figure 1 and Table 1 and don't change any conclusions in the paper (added on page 7).*

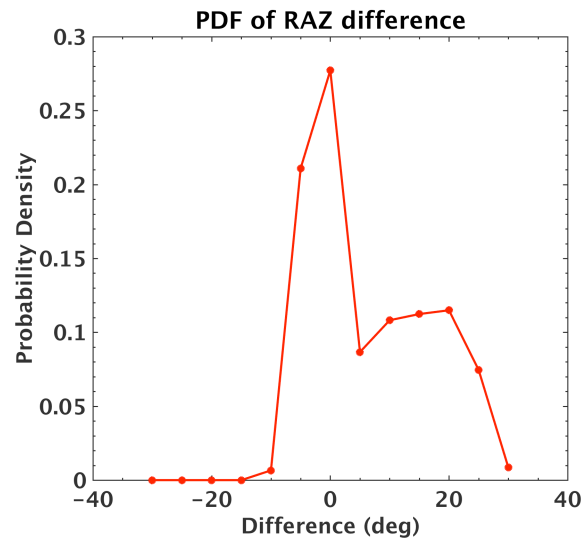
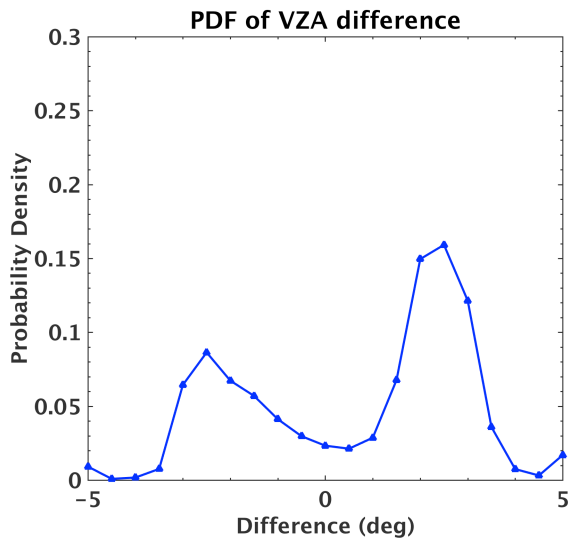


*To further illustrate that the SZA/VZA/RAZ matching criteria offer better angular matching than using scattering angle, we modified the SW footprint matching algorithm by using latitude and longitude differences less than 0.05 degree and scattering angle difference less than 2 degrees.*

The comparison of matched Aqua and NPP footprints are shown below. One thing we notice is that the number of matched footprints increased from 147,894 (Table 1) to 386,471, and the RMSE also increased from 4.1  $Wm^{-2}sr^{-1}$  to 4.7  $Wm^{-2}sr^{-1}$ .



The reason that the number of matched footprints increased so much is that using scattering angle difference  $< 2^\circ$  to match footprints can introduce some large VZA and RAZ differences. Plots below show the PDFs of VZA and RAZ differences when the scattering angle differences are less than 2 degrees (the SZA differences are always less than 0.5 degrees as the data we used are when both satellites flew in tandem). There are significant number of matched footprints have VZA differences greater than 2 degrees and RAZ differences greater than 5 degrees. The table below shows three case where scattering angle differences are less than 2 degrees, but the RAZ difference can be 40 degrees (first case), the VZA difference can be 20 degrees (last case).



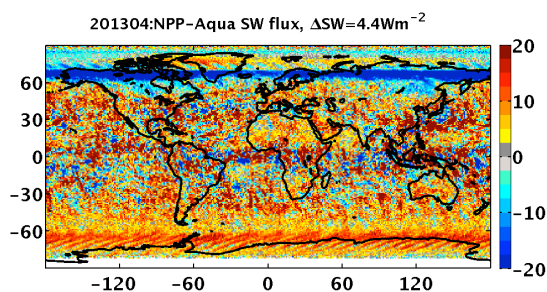
SZA	56.5	56.4	50.0	50.0	23.5	23.5
VZA	0.1	2.3	43.1	32.0	28.2	6.3
RAZ	157.1	116.3	71.5	74.0	51.2	52.5
Scat	56.6	57.4	50.5	48.9	22.1	20.3

We hope the above explanation can help the reviewer understand why we use SZA/VZA/RAZ angles to match the footprints instead of scattering angles.

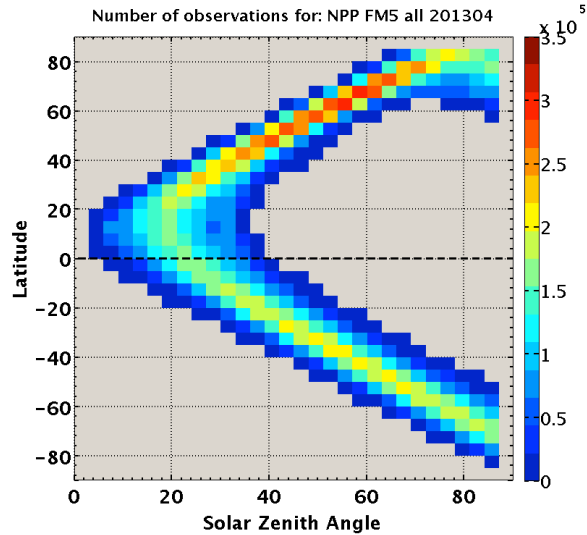
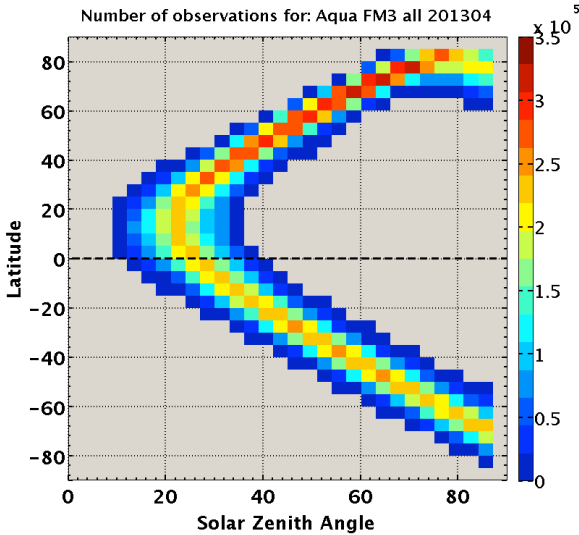
Figure 3 appears to contain an artifact such that it makes statements made in the paper invalid. Either correct the figure or explain the discrepancy / source of banding.

Figure 3: Can you please explain the source of the dark blue band of lower insolation around 60 deg. N? That almost looks like some kind of an artifact. Based on that banding artifact, your discussion on Page 8 that TOA fluxes track insolation differences is not valid. The TOA fluxes do not display any banding at 60 deg. N.

Figure 3 shows the monthly mean TOA insolation differences (NPP-Aqua), the monthly mean TOA reflected SW flux difference plot was not included in the paper, but was included in our first round response (shown below for reference). The TOA reflected SW flux difference plot clearly shows the same “dark blue” band as that in Figure 3. We don’t understand the reviewer’s statement “The TOA fluxes do not display any banding at 60 deg. N.”, as the “dark blue” band is definitely there. Maybe the reviewer is mistaken the albedo difference (Figure 4) for TOA flux difference.



The “dark blue” bands in both Figure 3 and the figure above are not an artifact, they are caused by the orbit differences between Aqua and S-NPP. Plots below shows the SZA density distributions for CERES-Aqua and CERES-NPP for different latitude zones for April 2013. At 60° N, the NPP overpasses at a lot more SZA>70 degrees than Aqua, which causes the solar insolation for NPP overpass time being smaller than that for Aqua, hence the TOA reflected SW flux (and this is why the “dark blue” band was not visible for the albedo plot). We modified a sentence on page 8 to reflect this fact: “Solar insolation for NPP overpass times are greater than that for Aqua overpass times over most regions, except over the northern high latitude where NPP has significantly more overpasses at  $\theta_0 > 70^\circ$  than Aqua”.



Minor comments:

Line 14: "... the imagers sharing the spacecraft with CERES-NPP... ."

*Modified.*

Line 91: reference for the IGBP dataset?

*Added.*

Line 98: Do you mean "VIIRS"? If not, please expand what VIRS stands for.

*Here VIRS (the Visible and Infrared Scanner) is the correct imager, it is already defined on line 51.*

Line 200: "... to be applicable to the VIIRS observations...."

*Modified.*

Line 207: "... was generated .... "

*Modified.*

Line 245: "... except for small differences ... "

*Modified.*

Line 365: "... the imagers sharing the spacecraft ... " They are mounted together, not flying in a constellation

*Modified as "there are some differences between the imagers that are on the same spacecrafts as CERES-Aqua (MODIS) and CERES-NPP (VIIRS)".*

Line 386: "... five years ...." no dash

*Modified to "five years".*

1 **The effects of different footprint sizes and cloud algorithms on the**  
2 **top-of-atmosphere radiative flux calculation from the Clouds and**  
3 **Earth's Radiant Energy System (CERES) instrument on**  
4 **Suomi-NPP**

5 WENYING SU, \*

*Science Directorate, NASA Langley Research Center, Hampton, Virginia*

6 LUSHENG LIANG, WALTER F. MILLER, VICTOR E. SOTHCOTT

*Science Systems & Applications, Inc., Hampton, Virginia*

---

\* *Corresponding author address:* Wenying Su, MS420, NASA Langley Research Center, Hampton, VA 23681.

E-mail: Wenying.Su-1@nasa.gov

## ABSTRACT

7  
8 Only one CERES instrument is onboard the Suomi-NPP and it has been placed in cross-track  
9 mode since launch, it is thus not possible to construct a set of angular distribution models  
10 (ADMs) specific for CERES on NPP. Edition 4 Aqua ADMs are used for flux inversions for  
11 CERES-NPP measurements. However, the footprint size of CERES-NPP is greater than  
12 that of CERES-Aqua, as the altitude of the NPP orbit is higher than that of the Aqua orbit.  
13 Furthermore, cloud retrievals from the Visible Infrared Imaging Radiometer Suite (VIIRS)  
14 and the Moderate Resolution Imaging Spectroradiometer (MODIS), **the imagers sharing the**  
15 **spacecrafts with CERES-NPP and CERES-Aqua, are also different.** To quantify the flux  
16 uncertainties due to the footprint size difference between CERES-Aqua and CERES-NPP,  
17 and due to both the footprint size difference and cloud property difference, a simulation  
18 is designed using the MODIS pixel level data which are convolved with the CERES-Aqua  
19 and CERES-NPP point spread functions into their respective footprints. The simulation is  
20 designed to isolate the effects of footprint size and cloud property differences on flux uncer-  
21 tainty from calibration and orbital differences between CERES-NPP and CERES-Aqua. The  
22 footprint size difference between CERES-Aqua and CERES-NPP introduces instantaneous  
23 flux uncertainties in monthly gridded CERES-NPP of less than  $4.0 \text{ Wm}^{-2}$  for SW, and less  
24 than  $1.0 \text{ Wm}^{-2}$  for both daytime and nighttime LW. The global monthly mean instanta-  
25 neous SW flux from simulated CERES-NPP has a low bias of  $0.4 \text{ Wm}^{-2}$  when compares  
26 to simulated CERES-Aqua, and the root-mean-square (RMS) error is  $2.2 \text{ Wm}^{-2}$  between  
27 them; the biases of daytime and nighttime LW flux are close to zero with RMS errors of  $0.8$   
28  $\text{Wm}^{-2}$  and  $0.2 \text{ Wm}^{-2}$ . These uncertainties are within the uncertainties of CERES ADMs.  
29 When both footprint size and cloud property (cloud fraction and optical depth) differences  
30 are considered, the uncertainties of monthly gridded CERES-NPP SW flux can be up to  
31  $20 \text{ Wm}^{-2}$  in the Arctic regions where cloud optical depth retrievals from VIIRS differ sig-  
32 nificantly from MODIS. The global monthly mean instantaneous SW flux from simulated  
33 CERES-NPP has a high bias of  $1.1 \text{ Wm}^{-2}$  and the RMS error increases to  $5.2 \text{ Wm}^{-2}$ . LW

34 flux shows less sensitivity to cloud property differences than SW flux, with the uncertainties  
35 of about  $2 \text{ Wm}^{-2}$  in monthly gridded LW flux, and the RMS errors of global monthly mean  
36 daytime and nighttime fluxes increase only slightly. These results highlight the importance  
37 of consistent cloud retrieval algorithms to maintain the accuracy and stability of the CERES  
38 climate data record.



# 1. Introduction

The Clouds and Earth’s Radiant Energy System (CERES) project has been providing data products critical to advancing our understanding of the effects of clouds and aerosols on radiative energy within the Earth-atmosphere system. CERES data are used by the science community to study the Earth’s energy balance (e.g., Trenberth et al. 2009; Kato et al. 2011; Loeb et al. 2012; Stephens et al. 2012), aerosol direct radiative effects (e.g., Satheesh and Ramanathan 2000; Zhang et al. 2005; Loeb and Manalo-Smith 2005; Su et al. 2013), aerosol-cloud interactions (e.g., Loeb and Schuster 2008; Quaas et al. 2008; Su et al. 2010b), and to evaluate global general circulation models (e.g., Pincus et al. 2008; Su et al. 2010a; Wang and Su 2013; Wild et al. 2013).

Six CERES instruments have flown on four different satellites thus far. CERES pre-Flight Model (FM) on Tropical Rainfall Measuring Mission (TRMM) was launched on November 27, 1997 into a 350-km circular precessing orbit with a 35° inclination angle and flew together with the Visible and Infrared Scanner (VIRS). CERES instruments (FM1 and FM2) on Terra were launched on December 18, 1999 into a 705-km sun-synchronous orbit with a 10:30 a.m. equatorial crossing time. CERES instruments (FM3 and FM4) on Aqua satellite were launched on May 4, 2002 into a 705-km sun-synchronous orbit with a 1:30 p.m. equatorial crossing time. CERES on Terra and Aqua flies alongside Moderate-Resolution Imaging Spectroradiometer (MODIS). CERES instrument (FM5) was launched onboard Suomi-NPP (hereafter referred to as NPP) on October 28, 2011 into a 824-km sun-synchronous orbit with a 1:30 p.m. equatorial crossing time and flies alongside the Visible Infrared Imaging Radiometer Suite (VIIRS). As the orbit altitudes differ among these satellites, the spatial resolutions of CERES instruments also vary from each other. TRMM has the lowest orbit altitude and offers the highest spatial resolution of CERES measurements, about 10 km at nadir; the spatial resolution of CERES on Terra and Aqua is about 20 km at nadir; and is about 24 km at nadir for NPP as it has the highest orbit altitude.

The CERES instrument consists of a three-channel broadband scanning radiometer (Wielicki

66 et al. 1996). The scanning radiometer measures radiances in shortwave (SW, 0.3-5  $\mu m$ ), win-  
 67 dow (WN, 8-12  $\mu m$ ), and total (0.3-200  $\mu m$ ) channels. The longwave (LW) component is  
 68 derived as the difference between total and SW channels. These measured radiances ( $I$ ) at  
 69 a given sun-Earth-satellite geometry are converted to outgoing reflected solar and emitted  
 70 thermal TOA radiative fluxes ( $F$ ) as:

$$F(\theta_0) = \frac{\pi I(\theta_0, \theta, \phi)}{R_j(\theta_0, \theta, \phi)}. \quad (1)$$

71 where  $\theta_0$  is the solar zenith angle,  $\theta$  is the CERES viewing zenith angle,  $\phi$  is the relative  
 72 azimuth angle between CERES and the solar plane, and  $R_j(\theta_0, \theta, \phi)$  is the anisotropic factors  
 73 for scene type  $j$ . Here scene type is a combination of variables (e.g., surface type, cloud  
 74 fraction, cloud optical depth, cloud phase, aerosol optical depth, precipitable water, lapse  
 75 rate, etc) that are used to group the data to develop distinct angular distribution models  
 76 (ADMs). Note the SW ADMs are developed as a function of  $\theta_0, \theta, \phi$  for each scene type,  
 77 whereas the LW ADMs are a weak function of  $\theta_0$  and  $\phi$  and are developed only as a function  
 78 of  $\theta$  (Loeb et al. 2005; Su et al. 2015a).

79 To facilitate the construction of ADMs, there are pairs of identical CERES instruments  
 80 on both Terra and Aqua. At the beginning of these missions one of the instruments on each  
 81 satellite was always placed in a rotating azimuth plane (RAP) scan mode, while the other  
 82 one was placed in cross-track mode to provide spatial coverage. When in RAP mode, the  
 83 instrument scans in elevation as it rotates in azimuth, thus acquiring radiance measurements  
 84 from a wide range of viewing combinations. There are about 60 months of RAP data collected  
 85 on Terra and about 32 months of RAP data collected on Aqua. CERES instruments fly  
 86 alongside high-resolution imagers, which provide accurate scene type information within  
 87 the CERES footprints. Cloud and aerosol retrievals based upon high-resolution imager  
 88 measurements are averaged over the CERES footprints by accounting for the CERES point  
 89 spread function (PSF, Smith 1994) and are used for scene type classification. Similarly,  
 90 spectral radiances from MODIS/VIIRS observations are averaged over the CERES footprints  
 91 weighted by the CERES PSF. Surface types are obtained from the International Geosphere

92 Biosphere Program (IGBP, Loveland and Belward 1997) global land cover data set. Fresh  
93 snow and sea ice surface types are derived from a combination of the National Snow and Ice  
94 Data Center (NSIDC) microwave snow/ice map and the National Environmental Satellite,  
95 Data and Information Service (NESDIS) snow/ice map. NESDIS uses imager data to identify  
96 snow and sea ice and provide snow and sea ice information near the coast, whereas NSIDC  
97 does not provide microwave retrievals within 50 km of the coast.

98 TRMM ADMs were developed using 9 months of CERES observations and the scene  
99 identification information retrieved from VIRS observations (Loeb et al. 2003). Terra ADMs  
100 and Aqua ADMs were developed separately using multi-year CERES Terra and Aqua mea-  
101 surements in RAP mode and in cross-track mode using the scene identification information  
102 from Terra MODIS and Aqua MODIS (Loeb et al. 2005; Su et al. 2015a). The high-resolution  
103 MODIS imager provides cloud conditions for every CERES footprint. The cloud algorithms  
104 developed by the CERES cloud working group retrieve cloud fraction, cloud optical depth,  
105 cloud phase, cloud top and effective temperature/pressure (among other variables) based on  
106 MODIS pixel-level measurements (Minnis et al. 2010). These pixel-level cloud properties  
107 are spatially and temporally matched with the CERES footprints and are used to select the  
108 scene-dependent ADMs to convert the CERES measured radiances to fluxes (Eq.1). The  
109 spatial matching criterion used is 1 km. The temporal matching criterion used is less than  
110 20 seconds when CERES is in cross-track mode, and less than 6 minutes when CERES is in  
111 RAP mode.

112 There is only one CERES instrument on NPP and it has been placed in cross-track scan  
113 mode since launch, it is thus not feasible to develop a specific set of ADMs for CERES  
114 on NPP. Currently, the Edition 4 Aqua ADMs (Su et al. 2015a) are used to invert fluxes  
115 for the CERES measurements on NPP. The CERES footprint size on NPP is larger than  
116 that on Aqua. As pointed out by Di Girolamo et al. (1998), the nonreciprocal behavior  
117 of the radiation field depends on measurement resolution, which means the ADMs do too.  
118 They concluded that ADMs should be applied only to data of the same resolution as the

119 data used to derive the ADMs. Since the footprint sizes are different between CERES-Aqua  
120 and CERES-NPP, will using ADMs developed based upon CERES-Aqua measurements for  
121 CERES-NPP flux inversion introduce any uncertainties in the CERES-NPP flux? Addition-  
122 ally, ADMs are scene type dependent, it is important to use consistent scene identification  
123 for developing and applying the ADMs. However, the VIIRS channels are not identical to  
124 those of MODIS, especially the lack of  $6.7 \mu\text{m}$  and  $13.3 \mu\text{m}$  channels, caused the cloud prop-  
125 erties retrieved from MODIS and VIIRS differ from each other. These differences affect the  
126 scene identification used to select the ADMs for flux inversion and thus can lead to addi-  
127 tional uncertainties in the CERES-NPP flux. In this study, we design a simulation study to  
128 quantify the CERES-NPP flux uncertainties due to the footprint size difference alone, and  
129 due to both the footprint size and cloud property differences.

## 130 **2. Comparison between CERES-Aqua and CERES-NPP**

131 Besides the altitude differences between Aqua and NPP satellites, they are also different  
132 in other orbital characteristics. For example, the orbital period for Aqua is about 98.82  
133 minutes, while it is about 101.44 minutes for NPP; and the orbital inclination for Aqua is  
134 about  $98.20^\circ$ , while it is about  $98.75^\circ$  for NPP. These orbital differences result in different  
135 local overpass times between Aqua and NPP and their orbits fly over each other about every  
136 64 hours. These simultaneous observations from Aqua and NPP are matched to compare  
137 SW and LW radiances using CERES Aqua Edition 4 Single Scanner Footprint TOA/Surface  
138 Fluxes and Clouds (SSF) product and CERES NPP Edition 1 SSF product. Here we use  $I_a^m$   
139 to denote the CERES-Aqua (subscript  $a$ ) measured (superscript  $m$ ) radiance, and  $I_n^m$  as the  
140 CERES-NPP (subscript  $n$ ) measured radiance. Similarly,  $F_a^m$  and  $F_n^m$  are the fluxes derived  
141 from  $I_a^m$  and  $I_n^m$  using CERES Aqua ADMs. The matching criteria used for SW radiances  
142 are that the latitude and longitude differences between the Aqua footprints and the NPP  
143 footprints are less than 0.05 degree, solar zenith angle and viewing zenith angle differences

144 are less than 2 degrees, and relative azimuth angle difference is less than 5 degrees. The  
145 matching criteria used here also provide a tight constraint on scattering angles, with about  
146 95.6% and 99.9% of the matched footprints having scattering angle differences less than  
147 2 degrees and 3 degrees. Same latitude and longitude matching criteria are used for LW  
148 radiances and the viewing zenith angle difference between the Aqua footprints and the NPP  
149 footprints is less than 2 degrees.

150 Figure 1 shows the SW, daytime LW, and nighttime LW radiance comparisons between  
151 CERES-Aqua and CERES-NPP using matched footprints of 2013 and 2014. The total  
152 number of matched footprints, the mean  $I_a^m$  and  $I_n^m$ , and the root-mean-square (RMS) errors  
153 are summarized in Table 1. The mean SW  $I_n^m$  is about  $1 \text{ Wm}^{-2}\text{sr}^{-1}$  greater than  $I_a^m$ , the mean  
154 daytime LW  $I_n^m$  is about  $0.4 \text{ Wm}^{-2}\text{sr}^{-1}$  smaller than  $I_a^m$ , and the nighttime LW  $I_n^m$  and  $I_a^m$   
155 agree to within  $0.1 \text{ Wm}^{-2}\text{sr}^{-1}$ . Excluding matched footprints with scattering angle difference  
156 greater than 2 degrees does not change the SW comparison result. These comparisons  
157 include data taken from nadir to oblique viewing angles ( $\theta > 60$ ). The RMS errors remain  
158 almost the same when we compare the radiances taken at different  $\theta$  ranges. Footprint size  
159 differences may also contribute to the radiance differences, but these radiance differences  
160 should be random. It is likely that the footprint size differences can increase the RMS errors,  
161 but the mean radiance differences are mostly resulted from calibration differences between  
162 CERES-Aqua and CERES-NPP. As mentioned earlier, the daytime CERES LW radiance  
163 is derived as the difference between total channel and SW channel measurements, and the  
164 nighttime CERES LW radiance is directly derived from the total channel measurements.  
165 The differences shown in Table 1 indicate that the agreement of the total channels between  
166 CERES-Aqua and CERES-NPP are better than that of the SW channels, leading to a smaller  
167 daytime LW difference than SW difference. Loeb et al. (2016) examined the normalized  
168 instrument gains for the total and SW channels for CERES FM1-FM5 since the beginning  
169 of the mission (BOM). The total channel response to LW radiation has gradually increased  
170 with time for all instruments. For the two instruments (FM3 and FM5) that are of interest

171 here, the increases relative to the BOM are 0.7% for FM3 and 0.4% for FM5. The SW  
172 channel response increases about 0.4% for FM3 and decreases by 0.2% for FM5. Exact  
173 causes for the calibration differences between CERES-Aqua and CERES-NPP are not yet  
174 known and more research are needed to understand their differences. The future plan is to  
175 place CERES-NPP on the same radiometric scale as CERES-Aqua.

176 Flux comparison using the same matched footprints are shown in Figure 2 and the mean  
177  $F_a^m$  and  $F_n^m$ , and the RMS errors between them are summarized in Table 1. Consistent with  
178 the radiance comparisons, the mean SW  $F_n^m$  is about  $3.8 \text{ Wm}^{-2}$  greater than  $F_a^m$ , the mean  
179 daytime LW  $F_n^m$  is about  $1.0 \text{ Wm}^{-2}$  smaller than  $F_a^m$ , and the mean nighttime LW  $F_n^m$  is  
180 about  $0.3 \text{ Wm}^{-2}$  smaller than  $F_a^m$ . When we compare the relative RMS errors (RMS error  
181 divided by the mean Aqua value) between radiance and flux, the relative flux RMS errors  
182 (6.4% for SW, 2.2% for daytime LW, and 1.4% for nighttime LW) are always slightly larger  
183 than the relative radiance RMS errors (6.0% for SW, 2.1% for daytime LW, and 1.1% for  
184 nighttime LW). This indicates that additional uncertainties are added when the radiances  
185 are converted to fluxes.

186 However, we cannot directly compare the gridded monthly mean fluxes from Aqua and  
187 NPP as their overpass times differ. Figure 3 shows the monthly mean TOA solar insolation  
188 difference between CERES-NPP and CERES-Aqua for April 2013. Solar insolation for NPP  
189 overpass times are greater than that for Aqua overpass times over most regions, except over  
190 the northern high latitude where NPP has significantly more overpasses at  $\theta_0 > 70^\circ$  than  
191 Aqua. Regional differences as large as  $30 \text{ Wm}^{-2}$  are observed over the tropical regions and  
192 north of  $60^\circ\text{N}$ . Globally, the CERES-NPP monthly mean solar insolation is greater than  
193 that of CERES-Aqua by  $13.4 \text{ Wm}^{-2}$  for this month. When we compare the monthly gridded  
194 TOA reflected SW flux between CERES-NPP and CERES-Aqua, most of the features re-  
195 semble those of the insolation differences (not shown). We thus compare the albedo between  
196 CERES-NPP and CERES-Aqua (Figure 4). Over most regions, the albedo from CERES-  
197 NPP is greater than that from CERES-Aqua, except over parts of tropical oceans and

198 Antarctica where some negative differences are observed. The global monthly mean albedo  
199 from CERES-NPP is greater than that from CERES-Aqua by 0.003 (1.02%). The albedo  
200 difference is mostly from the calibration differences (see Figure 1a), while the footprint size  
201 difference and scene identification difference also contribute to the albedo difference.

202 The CERES cloud working group developed sophisticated cloud detection algorithms  
203 using visible and infrared channels of MODIS separately for polar and non-polar regions and  
204 for daytime, twilight, and nighttime (Trepte et al. 2010). However, these detection algorithms  
205 have to be modified **to be applicable to the VIIRS observations** (Qing Trepte, personal  
206 communication), as some of the MODIS channels utilized for cloud detection are not available  
207 on VIIRS. These modifications include replacing the 2.1  $\mu\text{m}$  MODIS channel with the 1.6  
208  $\mu\text{m}$  VIIRS channel, and replacing detection tests using MODIS 6.7  $\mu\text{m}$  and 13.3  $\mu\text{m}$  channels  
209 with VIIRS 3.7  $\mu\text{m}$  and 11  $\mu\text{m}$  channels, and supplement with tests utilizing VIIRS 1.6  $\mu\text{m}$   
210 channel and the brightness temperature differences between 11  $\mu\text{m}$  and 12  $\mu\text{m}$ . These changes  
211 mainly affect the cloud detections over the polar regions. The parameterization of 1.24  
212  $\mu\text{m}$  reflectance **was regenerated** for VIIRS using improved wavelength and solar insolation  
213 weighting, which affects cloud optical depth retrieval over the snow/ice surfaces (Szedung  
214 Sun-Mack, personal communication). These changes result in different cloud properties  
215 retrieved using MODIS and VIIRS, especially over the polar regions. Figure 5 shows the  
216 daytime cloud fraction and cloud optical depth difference between VIIRS and Aqua-MODIS  
217 for April 2013. Cloud fraction retrieved from VIIRS is greater than that from MODIS by  
218 up to 10% and cloud optical depth from VIIRS is smaller than that from MODIS by 2~3  
219 over part of the Antarctic. Cloud fraction from VIIRS over the northern high-latitude snow  
220 regions is smaller than that from MODIS, while the optical depth from VIIRS is greater  
221 than that from MODIS. Over the Arctic, cloud optical depth from VIIRS is much larger  
222 than that from MODIS. Over the ocean between 60°S and 60°N, the differences in cloud  
223 fraction seem rather random while the differences in cloud optical depth is mostly positive  
224 (VIIRS retrieval is greater than Aqua-MODIS retrieval).

225 Given that the footprint sizes and overpass times are different between CERES-Aqua  
226 and CERES-NPP, in addition to the calibration differences and cloud retrieval differences  
227 between them, fluxes from these CERES instruments cannot be compared directly to assess  
228 the effects of footprint size difference and cloud property difference on flux uncertainty.

### 229 **3. Method**

230 To quantify the footprint size and cloud retrieval effect on flux inversion without having  
231 to account for the calibration and overpass time differences, we design a simulation study  
232 using the MODIS pixel level data and the Aqua-Earth-Sun geometry. MODIS spectral  
233 measurements are used to retrieve cloud properties and aerosol optical depth. These pixel-  
234 level imager-derived aerosol and cloud properties, and spectral narrowband (NB) radiances  
235 from MODIS are convolved with the CERES PSF to provide the most accurate aerosol and  
236 cloud properties that are spatially and temporally matched with the CERES broadband  
237 radiance data. Figure 6 illustrates the process of generating the simulated CERES-Aqua  
238 and CERES-NPP footprints from the MODIS pixels. We first use the CERES-Aqua PSF  
239 to convolve the aerosol/cloud properties, and the MODIS NB radiances (and other ancillary  
240 data) into Aqua-size footprints (left portion of Figure 6), as is done for the standard CERES-  
241 Aqua SSF product. These NB radiances for the simulated CERES-Aqua footprints are  
242 denoted as  $I_a^s(\lambda)$ , where superscript ‘s’ is for the simulated (in contrast to superscript ‘m’  
243 for the measured). We then increase the footprint size to be that of NPP and use the  
244 CERES-NPP PSF to average the MODIS NB radiances, cloud/aerosol properties, and other  
245 ancillary data into the simulated NPP footprints. NB radiances for the simulated CERES-  
246 NPP footprints are denoted as  $I_n^s(\lambda)$ .

247 Four months (July 2012, October 2012, January 2013, and April 2013) of simulated  
248 CERES-Aqua and CERES-NPP data were created. For every CERES-Aqua footprint, it  
249 contains the broadband SW and LW radiances measured by the CERES instrument. The



250 simulated NPP footprints, however, do not contain broadband radiances. To circumvent  
251 this issue, we developed narrowband-to-broadband coefficients to convert the MODIS NB  
252 radiances to broadband radiances.

253 The Edition 4 CERES-Aqua SSF data from July 2002 to September 2007 are used to  
254 derive the narrowband-to-broadband (NB2BB) regression coefficients separately for SW,  
255 daytime LW, and nighttime LW. Seven MODIS spectral bands (0.47, 0.55, 0.65, 0.86, 1.24,  
256 2.13, and 3.7  $\mu\text{m}$ ) are used to derive the broadband SW radiances, and the SW regression  
257 coefficients are calculated for every calendar month for discrete intervals of solar zenith angle,  
258 viewing zenith angle, relative azimuth angle, surface type, snow/non-snow conditions, cloud  
259 fraction, and cloud optical depth. Five MODIS spectral bands (6.7, 8.5, 11.0, 12.0, and 14.2  
260  $\mu\text{m}$ ) are used to derive the broadband LW radiances, and the LW regression coefficients are  
261 calculated for every calendar month for discrete intervals of viewing zenith angle, precipitable  
262 water, surface type, snow/none-snow conditions, cloud fraction, and cloud optical depth. The  
263 20 IGBP surface types are grouped into 8 surface types: ocean, forest, savanna, grassland,  
264 dark desert, bright desert, the Greenland permanent snow, and the Antarctic permanent  
265 snow. When there is sea ice over the ocean and snow over the land surface types, regression  
266 coefficients for ice and snow conditions are developed (only footprints with 100% sea ice/snow  
267 coverage are considered).

268 These SW and LW NB2BB regression coefficients are then applied to  $I_a^s(\lambda)$  and  $I_n^s(\lambda)$   
269 to derive the broadband radiances,  $I_a^s$  and  $I_n^s$ , for simulated footprints of CERES-Aqua  
270 and CERES-NPP, shown on the left and right of Figure 6, if the footprint consists of a  
271 single surface type. As both simulated CERES-Aqua and CERES-NPP footprints use the  
272 Aqua-Earth-Sun geometry,  $I_a^s$  and  $I_n^s$  have the same Sun-viewing geometry. Even though the  
273 CERES-Aqua footprints contained the broadband radiances from CERES observations ( $I_a^m$ ),  
274 we choose to use the broadband radiances calculated using the NB2BB regressions to ensure  
275 that  $I_a^s$  and  $I_n^s$  are consistently derived. Doing so we can isolate the flux differences between  
276 simulated CERES-Aqua and simulated CERES-NPP caused by footprint size difference.

277 The cloud properties in the simulated CERES-Aqua footprints and in the simulated  
278 CERES-NPP footprints are all based upon the MODIS retrievals, so the scene identifications  
279 used to select ADMs for flux inversion are almost the same for both the simulated CERES-  
280 Aqua and the CERES-NPP, **except for small differences** due to differing footprint sizes.  
281 As demonstrated in Figure 5, cloud properties differ between the MODIS and the VIIRS  
282 retrievals. These cloud retrieval differences affect the anisotropy factors selected for flux  
283 inversion. To simulate both the footprint size and cloud property differences, cloud fraction  
284 and cloud optical depth retrievals from MODIS convolved in the simulated CERES-NPP  
285 footprints are adjusted to be similar to those from VIIRS retrievals to assess how cloud  
286 retrieval differences affect the flux. To accomplish this, daily cloud fraction ratios of VIIRS  
287 to MODIS are calculated for each  $1^\circ$  latitude by  $1^\circ$  longitude grid box. These ratios are then  
288 applied to the cloudy footprints of MODIS retrieval to adjust the MODIS cloud fractions  
289 to be nearly the same as those from VIIRS retrieval. Note no adjustment is done for clear  
290 footprints. Similarly, daily cloud optical depth ratios of VIIRS to MODIS are calculated  
291 using cloudy footprints for each  $1^\circ$  by  $1^\circ$  grid box. These ratios are used to adjust the MODIS  
292 retrieved cloud optical depth to be close to those from VIIRS retrievals. **The process of gen-**  
293 **erating the simulated CERES-NPP footprints with VIIRS-like cloud retrievals is illustrated**  
294 **on the lower right portion of Figure 6.**

295 Aqua ADMs are then used to convert  $I_a^s$  and  $I_n^s$  to fluxes,  $F_a^s$  and  $F_n^s$ , for the simulated  
296 CERES-Aqua and CERES-NPP footprints using the cloud properties retrieved from MODIS  
297 observations for scene type identification. To further access the effects of both footprint size  
298 and cloud property differences on flux inversion, Aqua ADMs are used to convert  $I_n^s$  to flux,  
299  $F_n'^s$ , for the simulated CERES-NPP footprints using VIIRS-like cloud properties for scene  
300 identification.

## 4. Results

We first compare the footprint-level fluxes between simulated CERES-Aqua and simulated CERES-NPP using data of April 1, 2013 (about 700,000 footprints). As the cloud fraction and cloud optical depth adjustments are done at the grid box level, it is not feasible to compare footprint-level  $F'_n{}^s$  and  $F'_a{}^s$ , and only footprint-level  $F_n{}^s$  and  $F_a{}^s$  are compared. For SW, the bias between  $F'_a{}^s$  and  $F'_n{}^s$  is  $0.1 \text{ Wm}^{-2}$  and the RMS error is  $4.7 \text{ Wm}^{-2}$ . For LW, the biases is close to zero and the RMS errors are  $1.3 \text{ Wm}^{-2}$  and  $0.9 \text{ Wm}^{-2}$  for daytime and nighttime, respectively. These flux RMS errors are much smaller than those listed in Table 1, indicating that calibration differences are responsible for most of the flux differences between CERES-Aqua and CERES-NPP measurements. However, we should avoid direct comparisons between these two sets of RMS errors, as they are derived using different time period.

We now compare the monthly grid box ( $1^\circ$  latitude by  $1^\circ$  longitude) mean fluxes from the three simulations outlined in the previous section. Differences between  $F'_n{}^s$  and  $F'_a{}^s$  are used to assess the CERES-NPP gridded monthly mean instantaneous flux uncertainties due to the footprint size difference, and differences between  $F_n{}^s$  and  $F_a{}^s$  are used to assess the CERES-NPP gridded monthly mean instantaneous flux uncertainties due to both the footprint size and cloud property differences.

The monthly mean instantaneous TOA SW fluxes for simulated CERES-Aqua ( $F_a{}^s$ ) are shown in Figure 7(a) for April 2013. Note these fluxes are different from those in the Edition 4 Aqua SSF product as the CERES measured radiances differ from those inferred using NB2BB regression coefficients. The flux differences caused by the footprint size difference between the simulated CERES-NPP and the simulated CERES-Aqua ( $F_n{}^s - F_a{}^s$ ) are shown in Figure 7(b). Grid boxes in white indicate that the number of footprints with valid SW fluxes differ by more than 2% between simulated CERES-Aqua and CERES-NPP, as the NB2BB regressions are only applied to footprints that consist of the same surface types which result in fewer footprints with valid fluxes for CERES-NPP than for CERES-Aqua. The

328 footprint size difference between CERES-Aqua and CERES-NPP introduces an uncertainty  
329 that rarely exceeds  $4.0 \text{ Wm}^{-2}$  in monthly gridded CERES-NPP instantaneous SW fluxes.  
330 For global monthly mean instantaneous SW flux, the simulated CERES-NPP has a low bias  
331 of  $0.4 \text{ Wm}^{-2}$  compares to the simulated CERES-Aqua, and the RMS error between them is  
332  $2.4 \text{ Wm}^{-2}$ . Results from the other three months are very similar to April 2013 (not shown).

333 Figure 7(c) shows the SW flux difference caused by both the footprint size and cloud prop-  
334 erty differences ( $F_n^{s'} - F_a^s$ ). Adding the cloud property differences increase the CERES-NPP  
335 flux uncertainty comparing to when only footprint size differences are considered (Figure  
336 7(b)), monthly gridded instantaneous flux uncertainty over the Arctic ocean can exceed  $20$   
337  $\text{Wm}^{-2}$ . Accounting for cloud property differences, the global monthly mean instantaneous  
338 SW flux from simulated CERES-NPP has a high bias of  $1.1 \text{ Wm}^{-2}$  and the RMS error is  
339 increased to  $5.2 \text{ Wm}^{-2}$ . Over the Arctic Ocean, the cloud optical depth from VIIRS retrieval  
340 is much greater than that from the MODIS retrieval while the difference in cloud fraction is  
341 relatively small. Anisotropic factors for thick clouds are smaller than those for thin clouds  
342 at oblique viewing angles, and are larger for near-nadir viewing angles. The viewing ge-  
343 ometries over the Arctic Ocean produced more smaller anisotropic factors than larger ones  
344 when MODIS cloud optical depths were replaced with VIIRS-like cloud optical depths, which  
345 resulted in larger fluxes when using VIIRS-like cloud properties for flux inversion.

346 The daytime and nighttime LW flux from the simulated CERES-Aqua footprints, LW  
347 flux differences due to footprint size difference, and LW flux difference due to both footprint  
348 size difference and cloud property difference are shown in Figures 8 and 9. The effect of  
349 footprint size on gridded monthly mean daytime and nighttime LW flux is generally within  
350  $1.0 \text{ Wm}^{-2}$ . For global monthly mean LW flux, the differences between  $F_n^s - F_a^s$  are close to  
351 zero, and the RMS errors between them are about  $0.8 \text{ Wm}^{-2}$  and  $0.2 \text{ Wm}^{-2}$  for daytime  
352 and nighttime LW fluxes. When cloud property differences are also considered, their effect  
353 on gridded monthly mean LW fluxes increases to about  $2 \text{ Wm}^{-2}$ . The RMS errors of global  
354 monthly mean LW flux increase slightly to about  $0.9 \text{ Wm}^{-2}$  and  $0.5 \text{ Wm}^{-2}$  for daytime and

355 nighttime. The LW fluxes showed much less sensitivity to cloud property changes than the  
356 SW fluxes, especially over the Arctic Ocean where cloud optical depth changed significantly.  
357 This is because the LW ADMs over the snow/ice surfaces have very little sensitivity to cloud  
358 optical depth (Su et al. 2015a), but they were developed for discrete cloud fraction intervals  
359 and larger flux changes are noted in regions experiencing large cloud fraction changes.

## 360 5. Summary and discussion

361 The scene-type dependent ADMs are used to convert the radiances measured by the  
362 CERES instruments to fluxes. Specific empirical ADMs were developed for CERES instru-  
363 ments on TRMM, Terra, and Aqua (Loeb et al. 2003, 2005; Su et al. 2015a). As there is only  
364 one CERES instrument on NPP and it has been placed in cross-track mode since launch,  
365 it is not possible to construct a set of ADMs specific for CERES on NPP. Edition 4 Aqua  
366 ADMs (Su et al. 2015a) are thus used for flux inversions for CERES-NPP measurements.  
367 However, the altitude of the NPP orbit is higher than that of the Aqua orbit resulting in  
368 a larger CERES footprint size on NPP than on Aqua. Given that the footprint size of  
369 CERES-NPP is different from that of CERES-Aqua, we need to quantify the CERES-NPP  
370 flux uncertainty caused by using the CERES-Aqua ADMs. Furthermore, there are some  
371 differences between [the imagers that are on the same spacecrafts](#) as CERES-Aqua (MODIS)  
372 and CERES-NPP (VIIRS), as VIIRS lacks the  $6.7 \mu\text{m}$  and  $13.3 \mu\text{m}$  channels. These spectral  
373 differences and algorithm differences lead to notable cloud fraction and cloud optical depth  
374 differences retrieved from MODIS and VIIRS. As the anisotropy factors are scene-type de-  
375 pendent, differences in cloud properties will also introduce uncertainties in flux inversion.  
376 Furthermore, the calibrations between CERES instruments on Aqua and on NPP also are  
377 different from each other. Comparisons using two years of collocated CERES-Aqua and  
378 CERES-NPP footprints indicate that the SW radiances from CERES-NPP are about 1.5%  
379 greater than those from CERES-Aqua, the daytime LW radiances from CERES-NPP are

380 about 0.5% smaller than those from CERES-Aqua, and the nighttime LW radiances agree  
381 to within 0.1%.

382 To quantify the flux uncertainties due to the footprint size difference between CERES-  
383 Aqua and CERES-NPP, and due to both the footprint size difference and cloud property  
384 difference, we use the MODIS pixel level data to simulate the CERES-Aqua and CERES-  
385 NPP footprints. The simulation is designed to isolate the effects of footprint size differ-  
386 ence and cloud property difference on flux uncertainty from calibration difference between  
387 CERES-NPP and CERES-Aqua. The pixel-level MODIS spectral radiances, the imager-  
388 derived aerosol and cloud properties, and other ancillary data are first convolved with the  
389 CERES Aqua PSF to generate the simulated CERES-Aqua footprints, and then convolved  
390 with the CERES NPP PSF to generate the simulated CERES-NPP footprints. Broadband  
391 radiances within the simulated CERES-Aqua and CERES-NPP footprints are derived us-  
392 ing the MODIS spectral bands based upon narrowband-to-broadband regression coefficients  
393 developed using [five years](#) of Aqua data to ensure consistency between broadband radi-  
394 ances from simulated CERES-Aqua and CERES-NPP. These radiances are then converted  
395 to fluxes using the CERES-Aqua ADMs. The footprint size difference between CERES-Aqua  
396 and CERES-NPP introduces instantaneous flux uncertainties in monthly gridded CERES-  
397 NPP of less than  $4.0 \text{ Wm}^{-2}$  for SW, and less than  $1.0 \text{ Wm}^{-2}$  for both daytime and nighttime  
398 LW. The global monthly mean instantaneous SW flux from simulated CERES-NPP has a  
399 low bias of  $0.4 \text{ Wm}^{-2}$  compares to that from simulated CERES-Aqua, and the RMS error  
400 between them is  $2.4 \text{ Wm}^{-2}$ . The biases in global monthly mean LW fluxes are close to zero,  
401 and the RMS errors between simulated CERES-NPP and simulated CERES-Aqua are about  
402  $0.8 \text{ Wm}^{-2}$  and  $0.2 \text{ Wm}^{-2}$  for daytime and nighttime global monthly mean LW fluxes.

403 The cloud properties in the simulated CERES-Aqua footprints and in the simulated  
404 CERES-NPP footprints are all based upon MODIS retrievals, but in reality cloud prop-  
405 erties retrieved from VIIRS differ from those from MODIS. To assess the flux uncertainty  
406 from scene identification differences, cloud fraction and cloud optical depth in the simulated

407 CERES-NPP footprints are perturbed to be more like the VIIRS retrievals. When both  
408 footprint size and cloud property differences are considered, the uncertainties of monthly  
409 gridded CERES-NPP SW flux can be up to  $20 \text{ Wm}^{-2}$  in the Arctic regions where cloud  
410 optical depth retrievals from VIIRS differ significantly from MODIS. The global monthly  
411 mean instantaneous SW flux from simulated CERES-NPP has a high bias of  $1.1 \text{ Wm}^{-2}$  and  
412 the RMS error is increased to  $5.2 \text{ Wm}^{-2}$ . LW flux shows less sensitivity to cloud property  
413 differences than SW flux, with the uncertainties of about  $2.0 \text{ Wm}^{-2}$  in monthly gridded LW  
414 flux, and the RMS errors increases to  $0.9 \text{ Wm}^{-2}$  and  $0.5 \text{ Wm}^{-2}$  for daytime and nighttime  
415 LW flux.

416 Su et al. (2015b) quantified the global monthly 24hr-averaged flux uncertainties due to  
417 CERES ADMs using direct integration tests, and concluded that the RMS errors are less  
418 than  $1.1 \text{ Wm}^{-2}$  and  $0.8 \text{ Wm}^{-2}$  for 24hr-averaged TOA SW and LW fluxes. The uncertainty  
419 for global monthly instantaneous SW flux is approximately twice the uncertainty of 24hr-  
420 averaged flux. This simulation study indicates that the footprint size differences between  
421 CERES-NPP and CERES-Aqua introduce flux uncertainties that are within the uncertain-  
422 ties of the CERES ADMs. However, the uncertainty assessment provided here should be  
423 considered as the low end, as many regions (especially over land, snow, and ice) were not  
424 included due to sample number differences within the grid boxes. When cloud property  
425 differences are accounted for, the SW flux uncertainties increase significantly and exceed the  
426 uncertainties of the CERES ADMs. These findings indicate that inverting CERES-NPP flux  
427 using CERES-Aqua ADMs resulting in flux uncertainties that are within the ADMs uncer-  
428 tainties as long as the cloud retrievals between VIIRS and MODIS are consistent. When  
429 the cloud retrieval differences between VIIRS and MODIS are accounted for, the SW flux  
430 uncertainties exceed those of the CERES ADMs. To maintain the consistency of the CERES  
431 climate data record, it is thus important to develop cloud retrieval algorithms that account  
432 for the capabilities of both MODIS and VIIRS to ensure consistent cloud properties from  
433 both imagers.

435 *Acknowledgments.*

436 This research was supported by the NASA CERES project. The CERES data were ob-  
437 tained from the NASA Langley Atmospheric Science Data Center at [https://eosweb.larc.nasa.](https://eosweb.larc.nasa.gov/project/ceres/ssf_table)  
438 [gov/project/ceres/ssf\\_table](https://eosweb.larc.nasa.gov/project/ceres/ssf_table). We thank Norman Loeb, Szedung Sun-Mack, Qing Treppe, and  
439 Patrick Minnis for helpful discussions, and the three reviewers for their constructive com-  
440 ments and suggestions which have significantly improved this paper.



## REFERENCES

- 443 Di Girolamo, L., T. Varnai, and R. Davies, 1998: Apparent breakdown of reciprocity in  
444 reflected solar radiances. *J. Geophys. Res.*, **103 (D8)**, 8795–8803.
- 445 Kato, S., et al., 2011: Improvements of top-of-atmosphere and surface irradiance computa-  
446 tion with CALIPSO-, and MODIS-derived cloud and aerosol properties. *J. Geophys. Res.*,  
447 **116 (D19209)**, D19 209, doi:10.1029/2011JD016050.
- 448 Loeb, N. G., S. Kato, K. Loukachine, and N. Manalo-Smith, 2005: Angular distribution  
449 models for top-of-atmosphere radiative flux estimation from the clouds and the earth’s  
450 radiant energy system instrument on the terra satellite. part I: Methodology. *J. Atmos.*  
451 *Oceanic Technol.*, **22**, 338–351.
- 452 Loeb, N. G., J. M. Lyman, G. C. Johnson, R. P. Allan, D. R. Doelling, T. Wong, B. J.  
453 Soden, and G. L. Stephens, 2012: Observed changes in top-of-the-atmosphere radiation  
454 and upper-ocean heating consistent within uncertainty. *Nature Geosci.*, **5**, 110–113, doi:  
455 10.1038/NGEO1375.
- 456 Loeb, N. G. and N. Manalo-Smith, 2005: Top-of-atmosphere direct radiative effect of aerosols  
457 over global oceans from merged CERES and MODIS observations. *J. Climate*, **18**, 3506–  
458 3526.
- 459 Loeb, N. G., N. Manalo-Smith, S. Kato, W. F. Miller, S. K. Gupta, P. Minnis, and B. A.  
460 Wielicki, 2003: Angular distribution models for top-of-atmosphere radiative flux estima-  
461 tion from the Clouds and the Earth’s Radiant Energy System instrument on the Tropical  
462 Rainfall Measuring Mission satellite. Part I: Methodology. *J. Appl. Meteor.*, **42**, 240–265.

- 463 Loeb, N. G., N. Manalo-Smith, W. Su, M. Shankar, and S. Thomas, 2016: CERES top-of-  
464 atmosphere Earth radiation budget climate data record: Accounting for in-orbit changes  
465 in instrument calibration. *Remote Sens.*, **8 (182)**, doi:10.3390/rs8030182.
- 466 Loeb, N. G. and G. L. Schuster, 2008: An observational study of the relationship between  
467 cloud, aerosol and meteorology in broken low-level cloud conditions. *J. Geophys. Res.*,  
468 **113 (D14214)**, D14 214, doi:10.1029/2007JD009763.
- 469 Loveland, T. R. and A. S. Belward, 1997: The international geosphere biosphere programme  
470 data and information system global land cover dataset (DISCover). *Acta Astronaut.*, **41**,  
471 681–689.
- 472 Minnis, P., et al., 2010: CERES Edition 3 cloud retrievals. *13th Conference on Atmospheric*  
473 *Radiation*, Am. Meteorol. Soc., Oregon, Portland.
- 474 Pincus, R., C. P. Batstone, R. J. P. Hofmann, K. E. Taylor, and P. J. Glecker, 2008: Evalu-  
475 ating the present-day simulation of clouds, precipitation, and radiation in climate models.  
476 *J. Geophys. Res.*, **113 (D14209)**, D14 209, doi:10.1029/2007JD009334.
- 477 Quaas, J., O. Boucher, N. Bellouin, and S. Kinne, 2008: Satellite-based estimate of the  
478 direct and indirect aerosol climate forcing. *J. Geophys. Res.*, **113 (D05204)**, D05 204,  
479 doi:10.1029/2007JD008962.
- 480 Satheesh, S. K. and V. Ramanathan, 2000: Large differences in tropic aerosol forcing at  
481 the top of the atmosphere and earth’s surface. *Nature*, **405**, 60–63.
- 482 Smith, G. L., 1994: Effects of time response on the point spread function of a scanning  
483 radiometer. *Appl. Opt.*, **33**, 7031–7037.
- 484 Stephens, G. L., et al., 2012: An update on Earth’s energy balance in light of the latest  
485 global observations. *Nature Geosci.*, **5**, 691–696, doi:10:1038/NGEO1580.

- 486 Su, W., A. Bodas-Salcedo, K.-M. Xu, and T. P. Charlock, 2010a: Comparison of the trop-  
487 ical radiative flux and cloud radiative effect profiles in a climate model with Clouds and  
488 the Earth’s Radiant Energy System (CERES) data. *J. Geophys. Res.*, **115** (D01105),  
489 D01 105, doi:10.1029/2009JD012490.
- 490 Su, W., J. Corbett, Z. A. Eitzen, and L. Liang, 2015a: Next-generation angular distribution  
491 models for top-of-atmosphere radiative flux calculation from the CERES instruments:  
492 Methodology. *Atmos. Meas. Tech.*, **8**, 611–632, doi:10.5194/amt-8-611-2015.
- 493 Su, W., J. Corbett, Z. A. Eitzen, and L. Liang, 2015b: Next-generation angular distribution  
494 models for top-of-atmosphere radiative flux calculation from the CERES instruments:  
495 Validation. *Atmos. Meas. Tech.*, **8**, 3297–3313, doi:10.5194/amt-8-3297-2015.
- 496 Su, W., N. G. Loeb, G. L. Schuster, M. Chin, and F. G. Rose, 2013: Global all-sky shortwave  
497 direct radiative forcing of anthropogenic aerosols from combined satellite observations and  
498 GOCART simulations. *J. Geophys. Res.*, **118**, 1–15, doi:10.1029/2012JD018294.
- 499 Su, W., N. G. Loeb, K. Xu, G. L. Schuster, and Z. A. Eitzen, 2010b: An estimate of aerosol  
500 indirect effect from satellite measurements with concurrent meteorological analysis. *J.*  
501 *Geophys. Res.*, **115** (D18219), D18 219, doi:10.1029/2010JD013948.
- 502 Trenberth, K. E., J. T. Fasullo, and J. Kiehl, 2009: Earth’s global energy budget. *Bull. Am.*  
503 *Meteor. Soc.*, **90**, 311–323, doi:10.1175/2008BAMS2634.1.
- 504 Trepte, Q. Z., P. Minnis, C. Trepte, and S. Sun-Mack, 2010: Improved cloud detections in  
505 CERES Edition 3 algorithm and comparison with the CALIPSO vertical feature mask.  
506 *13th Conference on Atmospheric Radiation*, Am. Meteorol. Soc., Oregon, Portland.
- 507 Wang, H. and W. Su, 2013: Evaluating and understanding top of the atmosphere cloud  
508 radiative effects in Intergovernmental Panel on Climate Change (IPCC) fifth assessment  
509 report (AR5) coupled model intercomparison project phase 5 (CMIP5) models using  
510 satellite observations. *J. Geophys. Res.*, **118**, 1–17, doi:10.1029/2012JD018619.

- 511 Wielicki, B. A., B. R. Barkstrom, E. F. Harrison, R. B. Lee, G. L. Smith, and J. E. Cooper,  
512 1996: Clouds and the Earth's Radiant Energy System (CERES): An Earth Observing  
513 System experiment. *Bull. Amer. Meteor. Soc.*, **77**, 853–868.
- 514 Wild, M., D. Folini, C. Schar, N. G. Loeb, E. G. Dutton, and G. Konig-Langlo, 2013:  
515 The global energy balance from a surface perspective. *Clim. Dyn.*, **40**, 3107–3134, doi:  
516 10.1007/s00382-012-1569-8.
- 517 Zhang, J., S. A. Christopher, L. A. Remer, and Y. J. Kaufman, 2005: Shortwave aerosol  
518 radiative forcing over cloud-free oceans from Terra: 2. Seasonal and global distributions.  
519 *J. Geophys. Res.*, **110 (D10S24)**, D10S24, doi:10.1029/2004JD005009.

520 **List of Tables**

521 1 Comparison of CERES-Aqua and CERES-NPP measured SW, daytime LW,  
522 and nighttime LW radiances ( $\text{Wm}^{-2}\text{sr}^{-1}$ ) and fluxes ( $\text{Wm}^{-2}$ ) using matched  
523 footprints of 2013 and 2014. 24

TABLE 1. Comparison of CERES-Aqua and CERES-NPP measured SW, daytime LW, and nighttime LW radiances ( $\text{Wm}^{-2}\text{sr}^{-1}$ ) and fluxes ( $\text{Wm}^{-2}$ ) using matched footprints of 2013 and 2014.

	SW	Daytime LW	Nighttime LW
Sample Number	147894	192178	187880
Mean CERES-Aqua Radiance	68.1	77.4	74.4
Mean CERES-NPP Radiance	69.2	77.0	74.3
Radiance RMS Error	4.1	1.6	0.8
Mean CERES-Aqua Flux	230.1	235.7	226.4
Mean CERES-NPP Flux	233.9	234.7	226.1
Flux RMS Error	14.6	5.0	3.1

## 524 List of Figures

- 525 1 Radiance comparisons between matched CERES-Aqua and CERES-NPP foot-  
526 prints, (a) SW; (b) daytime LW; and (c) nighttime LW using data of 2013  
527 and 2014. 27
- 528 2 Flux comparisons between matched CERES-Aqua and CERES-NPP foot-  
529 prints, (a) SW; (b) daytime LW; and (c) nighttime LW using data of 2013  
530 and 2014. 28
- 531 3 Monthly mean solar insolation difference ( $\text{Wm}^{-2}$ ) between CERES-NPP and  
532 CERES-Aqua (NPP-Aqua) for April 2013. 29
- 533 4 Monthly mean albedo difference between CERES-NPP and CERES-Aqua  
534 (NPP-Aqua) for April 2013. 30
- 535 5 Cloud fraction (a) and cloud optical depth (b) differences between VIIRS and  
536 MODIS (VIIRS-MODIS) retrievals for April 2013. 31
- 537 6 Schematic diagram of convoluting the MODIS pixels into the simulated Aqua  
538 and NPP footprints. Left depicts the processes involved in producing the  
539 simulated Aqua footprints; middle for simulated NPP footprints with MODIS  
540 retrievals; and right for simulated NPP footprints with VIIRS-like retrievals. 32
- 541 7 The gridded monthly mean TOA instantaneous SW fluxes from the simulated  
542 Aqua footprints ( $F_a^s$ , a), the flux differences caused by footprint size difference  
543 between simulated NPP and simulated Aqua ( $F_n^s - F_a^s$ , b), and the flux differ-  
544 ences caused by both footprint size and cloud property differences ( $F_n'^s - F_a^s$ ,  
545 c) using April 2013 data. Regions shown in white have large sample number  
546 differences between simulated Aqua and simulated NPP. 33

- 547 8 The gridded monthly mean TOA daytime LW fluxes from the simulated Aqua  
548 footprints ( $F_a^s$ , a), the flux differences caused by footprint size difference be-  
549 tween simulated NPP and simulated Aqua ( $F_n^s - F_a^s$ , b), and the flux differ-  
550 ences caused by both footprint size and cloud property differences ( $F_n'^s - F_a^s$ ,  
551 c) using April 2013 data. Regions shown in white have large sample number  
552 differences between simulated Aqua and simulated NPP. 34
- 553 9 The gridded monthly mean TOA nighttime LW fluxes from the simulated  
554 Aqua footprints ( $F_a^s$ , a), the flux differences caused by footprint size difference  
555 between simulated NPP and simulated Aqua ( $F_n^s - F_a^s$ , b), and the flux differ-  
556 ences caused by both footprint size and cloud property differences ( $F_n'^s - F_a^s$ ,  
557 c) using April 2013 data. Regions shown in white have large sample number  
558 differences between simulated Aqua and simulated NPP. 35



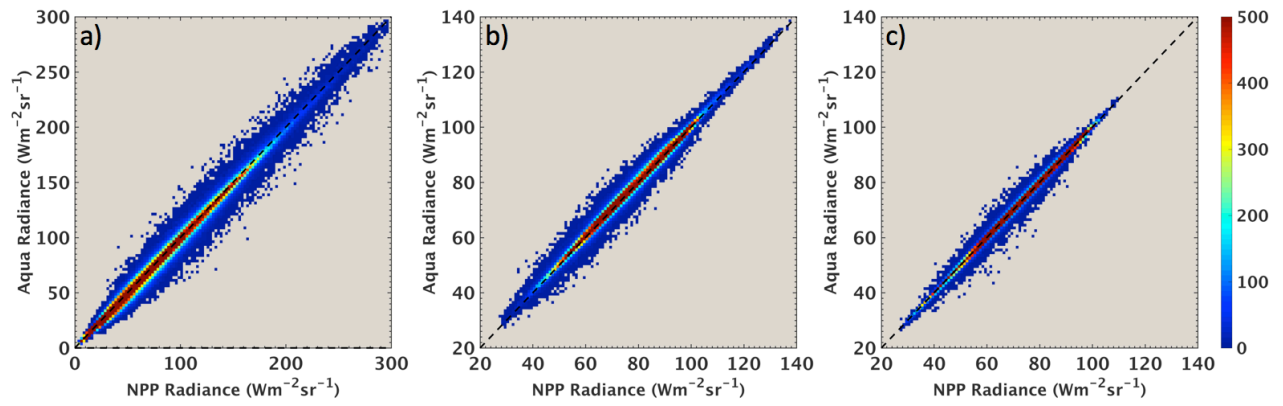


FIG. 1. Radiance comparisons between matched CERES-Aqua and CERES-NPP footprints, (a) SW; (b) daytime LW; and (c) nighttime LW using data of 2013 and 2014.

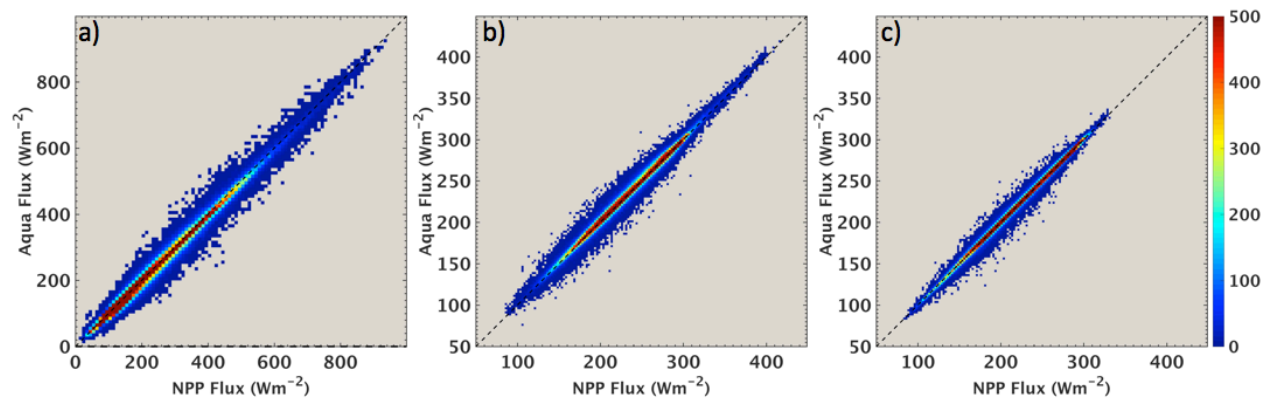


FIG. 2. Flux comparisons between matched CERES-Aqua and CERES-NPP footprints, (a) SW; (b) daytime LW; and (c) nighttime LW using data of 2013 and 2014.

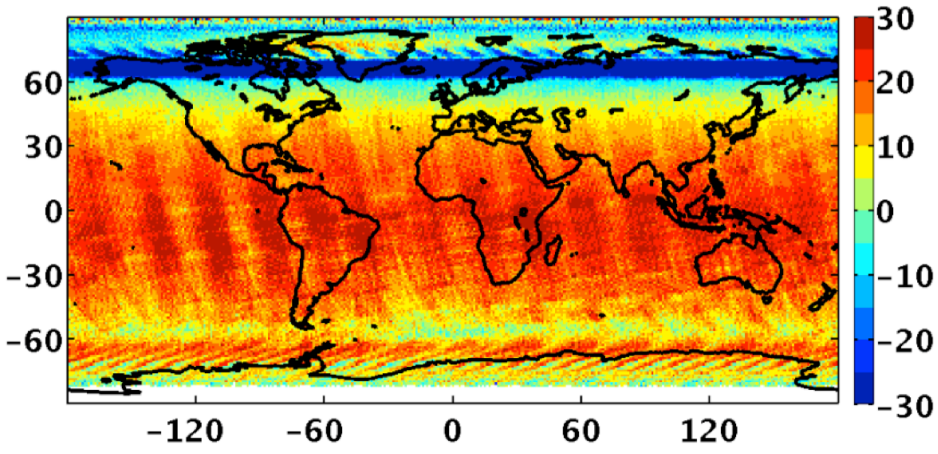


FIG. 3. Monthly mean solar insolation difference ( $\text{Wm}^{-2}$ ) between CERES-NPP and CERES-Aqua (NPP-Aqua) for April 2013.

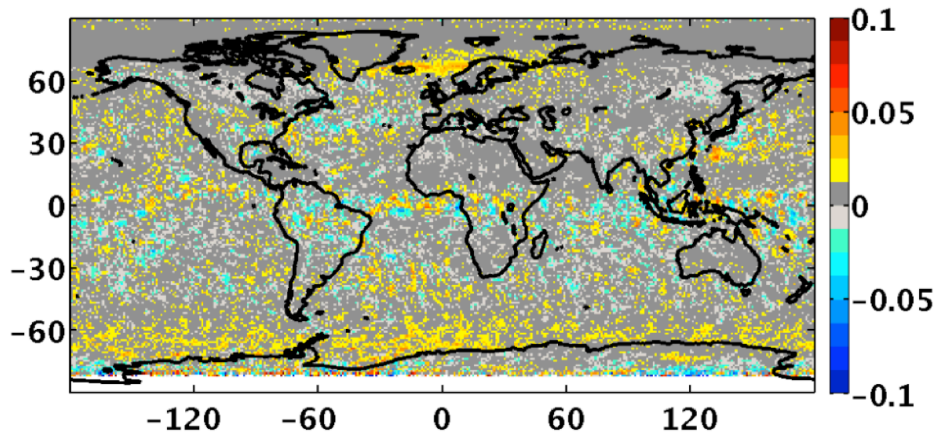


FIG. 4. Monthly mean albedo difference between CERES-NPP and CERES-Aqua (NPP-Aqua) for April 2013.

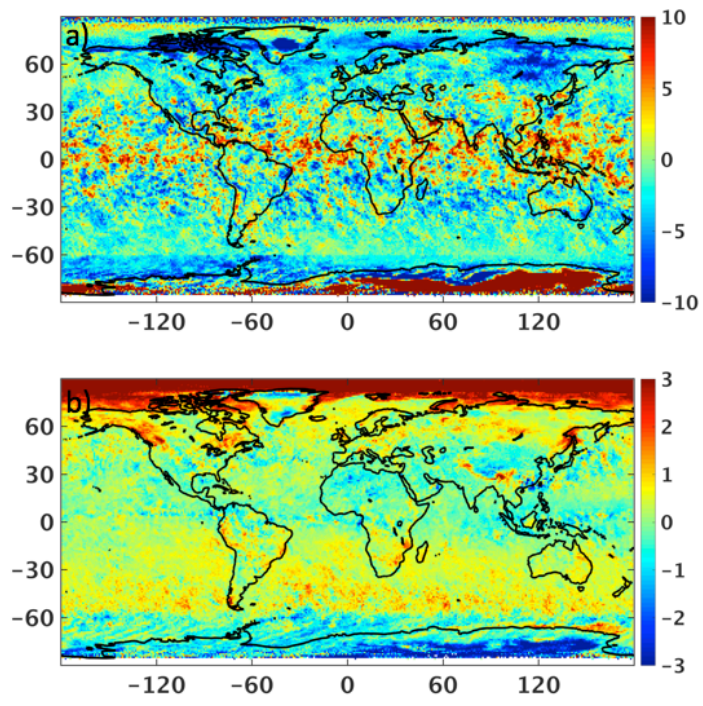


FIG. 5. Cloud fraction (a) and cloud optical depth (b) differences between VIIRS and MODIS (VIIRS-MODIS) retrievals for April 2013.

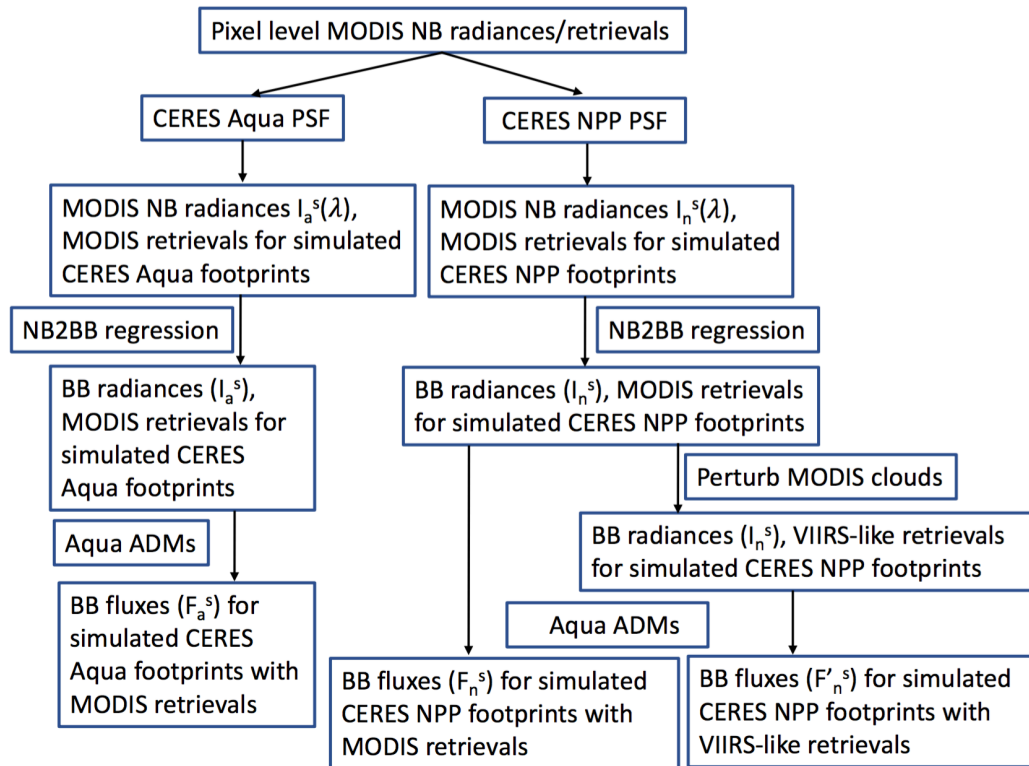


FIG. 6. Schematic diagram of convoluting the MODIS pixels into the simulated Aqua and NPP footprints. Left depicts the processes involved in producing the simulated Aqua footprints; middle for simulated NPP footprints with MODIS retrievals; and right for simulated NPP footprints with VIIRS-like retrievals.

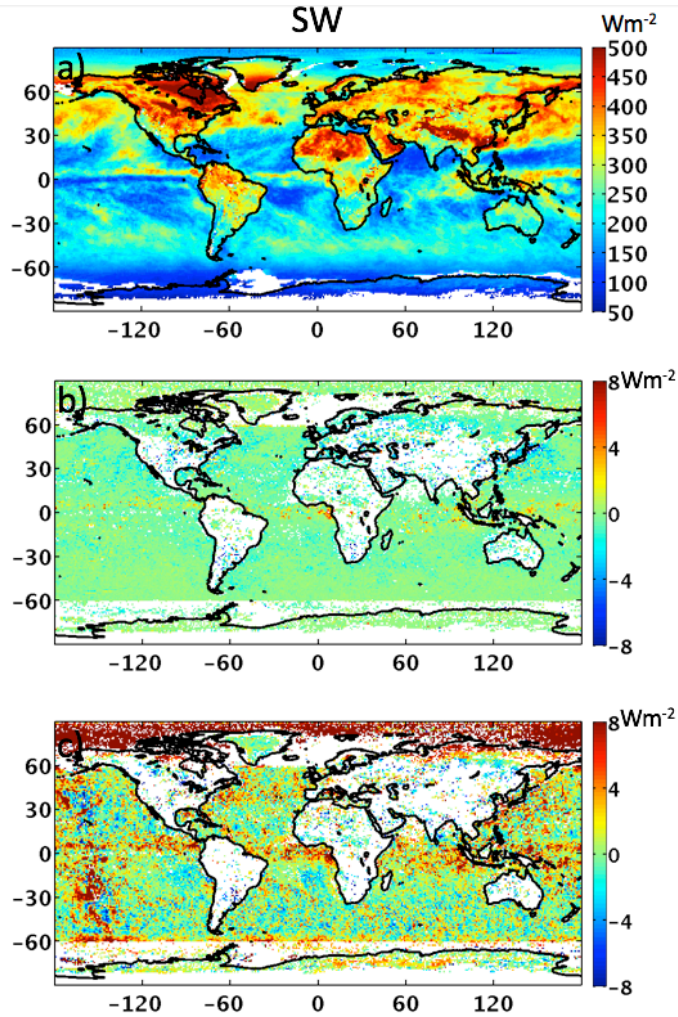


FIG. 7. The gridded monthly mean TOA instantaneous SW fluxes from the simulated Aqua footprints ( $F_a^s$ , a), the flux differences caused by footprint size difference between simulated NPP and simulated Aqua ( $F_n^s - F_a^s$ , b), and the flux differences caused by both footprint size and cloud property differences ( $F_n'^s - F_a^s$ , c) using April 2013 data. Regions shown in white have large sample number differences between simulated Aqua and simulated NPP.

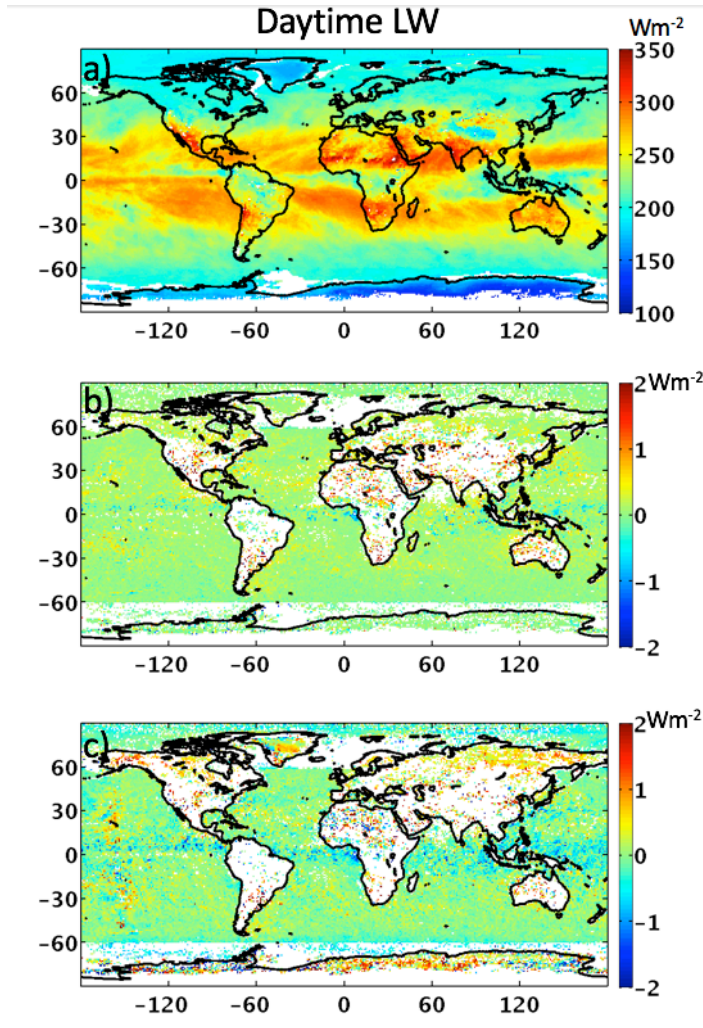


FIG. 8. The gridded monthly mean TOA daytime LW fluxes from the simulated Aqua footprints ( $F_a^s$ , a), the flux differences caused by footprint size difference between simulated NPP and simulated Aqua ( $F_n^s - F_a^s$ , b), and the flux differences caused by both footprint size and cloud property differences ( $F_n'^s - F_a^s$ , c) using April 2013 data. Regions shown in white have large sample number differences between simulated Aqua and simulated NPP.



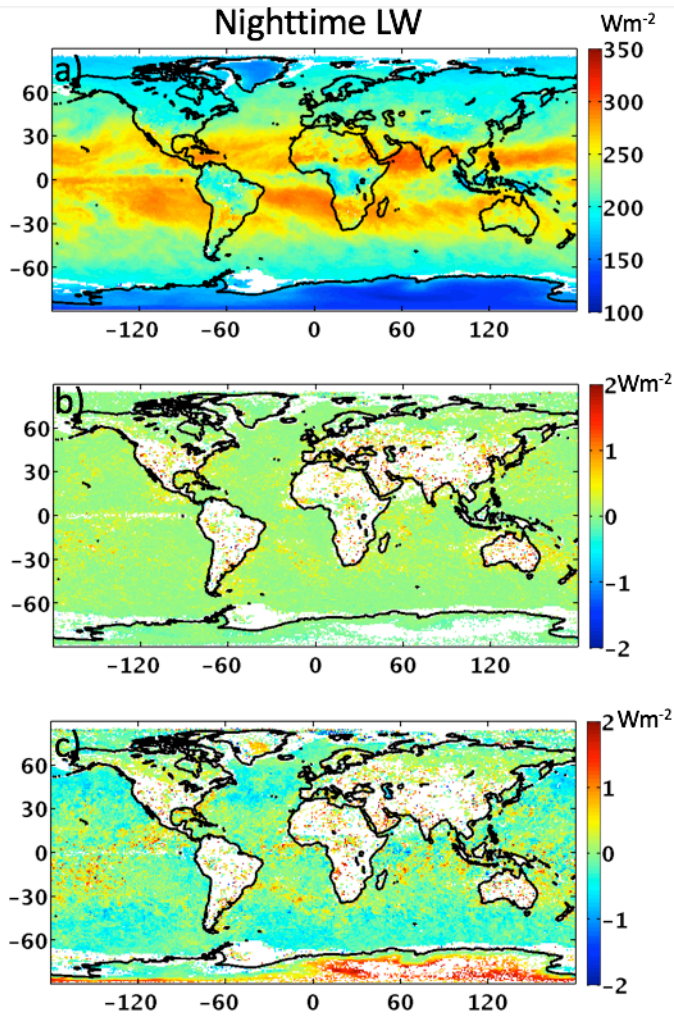


FIG. 9. The gridded monthly mean TOA nighttime LW fluxes from the simulated Aqua footprints ( $F_a^s$ , a), the flux differences caused by footprint size difference between simulated NPP and simulated Aqua ( $F_n^s - F_a^s$ , b), and the flux differences caused by both footprint size and cloud property differences ( $F_n'^s - F_a^s$ , c) using April 2013 data. Regions shown in white have large sample number differences between simulated Aqua and simulated NPP.